International Journal of Multiphase Flow 129 (2020) 103291

Contents lists available at ScienceDirect

International Journal of Multiphase Flow

journal homepage: www.elsevier.com/locate/ijmulflow

Sedimentation of finite-size particles in quiescent wall-bounded shear-thinning and Newtonian fluids

Dhiya Alghalibi[a,b,*], Walter Fornari[a], Marco E. Rosti[a,c], Luca Brandt[a]

[a] Linné Flow Centre and SeRC Swedish e-Science Research Centre,KTH Mechanics, Stockholm S-100 44, Sweden
[b] College of Engineering, University of Kufa, Al Najaf, Iraq
[c] Complex Fluids and Flows Unit, Okinawa Institute of Science and Technology Graduate University, 1919-1 Tancha, Onna-son, Okinawa 904-0495, Japan

ARTICLE INFO

Article history:
Received 16 May 2019
Revised 16 March 2020
Accepted 22 March 2020
Available online 25 April 2020

Keywords:
Shear-thinning
Particle sedimentation
Suspensions
Settling velocity
Multiphase

ABSTRACT

We study the sedimentation of finite-size particles in quiescent wall-bounded Newtonian and shear-thinning fluids by interface resolved numerical simulations. The suspended phase consists of Non-Brownian rigid spherical particles with particle to fluid density ratio $\rho_p/\rho_f = 1.5$ at three different solid volume fractions $\Phi = 1\%$, 5% and 20%. Firstly, to focus on the effect of shear-thinning on the particle dynamics and interactions, the Archimedes number is increased for a single particle to have the same settling speed in the Newtonian fluid as in the shear-thinning fluid. Secondly, we consider fixed Archimedes and vary the shear-thinning properties of the fluid. Overall, we report a twofold effect of shear thinning. First and more important, the substantial increase of the particle sedimentation velocity in the shear-thinning case due to the increase of the shear rate around the particles, which reduces the local viscosity leading to a reduced particle drag. Secondly, the shear-thinning fluid reduces the level of particle interactions, causing a reduction of velocity fluctuations and resulting in particles sedimenting at approximately the same speed. Moreover, the mean settling velocities decrease with the particle concentration as a consequence of the hindering effect. Particles tend to sediment in the middle of the channel, preferentially positioning in the wake of neighbouring particles or aside them, resulting in lower levels of fluid velocity fluctuations in the gravity direction in the shear-thinning fluid.

1. Introduction

The understanding of the settling of particles by the action of gravity through Newtonian and non-Newtonian carrier fluids is extremely important in many applications. Typical applications are found in environmental, biological and industrial applications such as studies of sand storm, pollutant transport in underground water, settling of micro-organisms such as plankton, as well as river sediment transport and the motion of drilling muds in boreholes. In these applications, the general problem of sedimentation of particles is a very complex one, due to the wide range of parameters upon which it depends. Sedimentation usually includes a high number of particles settling in various kind of environments. The fluid in which the particles are suspended may be quiescent or turbulent, wall-bounded or unbounded, Newtonian or non-Newtonian. Moreover, the particles may differ in shape, size, deformability or stiffness, density and particle concentrations, as well as for the large variety of interactions among them such as hydrodynamic, contact and interparticle forces. The interplay between these various parameters results in a wide range of spatial and temporal scales involved, substantially altering the global properties of these suspensions from one case to another. Because of these complexities and challenges, our general understanding of the problem is still incomplete. In this work we employ fully resolved direct numerical simulations, based on an efficient immersed boundary method, to study the behavior of monodisperse rigid spheres settling in quiescent wall-bounded Newtonian and shear-thinning fluids for different concentrations.

The sedimentation of an isolated spherical and non-spherical particle through Newtonian and non-Newtonian fluids has been extensively examined in the past, see e.g. Refs. Clift et al. (2005) and Chhabra (2006). The earliest investigations of the sedimentation of a single rigid sphere in an unbounded quiescent Newtonian fluid at zero Reynolds number focused on the Stokes analysis, where the particle terminal velocity was linked to the particle radius, the difference between the solid and fluid density and the fluid viscosity. Since then, several studies extended

* Corresponding author.
E-mail address: dhiya@mech.kth.se (D. Alghalibi).

https://doi.org/10.1016/j.ijmultiphaseflow.2020.103291
0301-9322/

the Stokes law by investigating the effects of additional parameters such as non-Newtonian media, particle shapes, nonzero Reynolds number, interactions between particles, and the effect of walls (e.g. Shah et al., 2007; Putz et al., 2008; Rajitha et al., 2006; Hsu et al., 2005; Turton and Clark, 1987; Kelessidis, 2004; Becker et al., 1996; Zhang et al., 2016). When the concentration of particles is increased, the motion and the settling velocity of an individual sedimenting object is affected by the existence of the others: this leads to a decrease of the mean settling velocity of the suspension, due to the so-called hindering effect (Davis and Acrivos, 1985). The hindering effect monotonically increases as a function of the solid volume fraction Φ, hence, the mean settling velocity is monotonically decreasing with Φ. One of the first experimental results for quiescent sedimentation under Newtonian flow conditions were those by Richardson and Zaki (1954). These authors proposed an empirical law relating the mean particle settling velocity of a suspension to its solid concentration and to the terminal velocity of a single particle. This formula is believed to be accurate also for high concentrated suspensions and has been improved by more recent experimental and numerical investigations in order to be applied at finite Reynolds numbers regimes (Garside and Al-Dibouni, 1977; Di Felice, 1999; Yin and Koch, 2007).

Efficient numerical methods and sufficient computational power to extract the average properties and the micro-structure of these particle suspensions have become available only recently and different algorithms have been successfully used (e.g. Ladd, 1993; Johnson and Tezduyar, 1996; Climent and Maxey, 2003; Yin and Koch, 2007; Pignatel et al., 2011; Uhlmann and Doychev, 2014). In particular, thanks to the immersed boundary method, it has been possible to obtain new insight on the interactions among the different phases and the resulting sedimenting suspension microstructure (Uhlmann and Doychev, 2014; Fornari et al., 2016; 2018; 2019). Fornari et al. (2018) simulated and studied the effect of the Galileo number (namely the ratio between gravitational and viscous forces) and volume fraction on the microscopic and macroscopic properties of settling rigid oblates in a quiescent Newtonian fluid at finite Reynolds number and for different solid volume fractions ($\Phi = 0.5\% - 10\%$).

The behaviour of many particles settling in a complex fluid is a less studied problem (Izbassarov et al., 2018). Only a few experimental and numerical studies have been devoted to the sedimentation of finite-size particle suspensions in quiescent non-Newtonian fluids, and the topic remains therefore poorly understood. It was observed in experimental investigations at low Reynolds number that the settling particles cluster to form columns or chains and cause the development of non-homogeneous structures during the sedimentation in either a shear-thinning fluid (Allen and Uhlherr, 1989; Bobroff and Phillips, 1998; Daugan et al., 2004) or a viscoelastic fluid (Allen and Uhlherr, 1989; Joseph et al., 1994; Bobroff and Phillips, 1998). In particular, the aggregation of the particles has been numerically examined in a viscoelastic fluid (Yu et al., 2002) and in a thixotropic shear-thinning fluid (an inelastic shear-thinning fluid with memory) (Yu et al., 2006).

Here, we investigate numerically the effect of a shear-thinning fluid on the settling behaviour of suspensions in a quiescent wall-bounded environment with finite particle Reynolds number for three different solid volume fractions ($\Phi = 1\%, 5\%, 20\%$) and compare the results with those obtained in a Newtonian fluid. In particular, we explore the mean particle settling and fluid velocities, the standard deviation of the different velocities, wall effects and microstructure of these complex suspensions. The present paper is organised as follows: the governing equations, numerical method and simulations setup are introduced in Section 2; the main results are discussed in Section 3, and the final remarks summarised in Section 4.

2. Methodology

2.1. Governing equations

We study the motion of finite-size rigid spheres settling in Newtonian and shear-thinning carrier fluids. The generalised incompressible Navier–Stokes equation with shear-dependent viscosity and the continuity equation govern the motion of the fluid phase,

$$\frac{\partial \mathbf{u}}{\partial t} + \mathbf{u}\cdot\nabla\mathbf{u} = -\frac{1}{\hat{\rho}_f}\nabla P + \nabla\cdot\left[\hat{\nu}(\mathbf{u})\left(\nabla\mathbf{u} + \nabla\mathbf{u}^T\right)\right] + \mathbf{f}, \tag{1a}$$

$$\nabla\cdot\mathbf{u} = 0, \tag{1b}$$

where $\mathbf{u} = (u, v, w)$ is the velocity vector with components in the (x, y, z) coordinate directions (see Fig. 1). The pressure is denoted by P while the fluid density and kinematic viscosity are indicated by $\hat{\rho}_f$ and $\hat{\nu} = \hat{\mu}/\hat{\rho}_f$ ($\hat{\mu}$ is the dynamic viscosity). The fluid viscosity, $\hat{\nu}$, is a constant for the Newtonian fluid, whereas it varies as a function of the local shear rate, $\dot{\gamma}(\mathbf{u})$, following the rheological Carreau-law defined below. Finally the body force $\mathbf{f}$ indicates the forcing from the dispersed phase on the carrier fluid.

The motion of the rigid spherical particles is described by the Newton-Euler equations,

$$\hat{\rho}_p V_p \frac{d\mathbf{U}_c^p}{dt} = \mathbf{F}_p, \tag{2a}$$

$$I_p \frac{d\mathbf{\Omega}_c^p}{dt} = \mathbf{T}_p, \tag{2b}$$

where $\mathbf{U}_c^p$ and $\mathbf{\Omega}_c^p$ are the translational and angular velocities of the particle p, while $\hat{\rho}_p$, $V_p = 4\pi a^3/3$ and $I_p = 2\hat{\rho}_p V_p a^2/5$ are the mass density, volume and moment-of-inertia of a sphere with radius a. $\mathbf{F}_p$ and $\mathbf{T}_p$ are the net force and momentum resulting from the hydrodynamic stresses on the particle surface, gravity and particle-particle interactions,

$$\mathbf{F}_p = \oint_{\partial S_p}\left[-P\mathbf{I} + \hat{\mu}(\mathbf{u})\left(\nabla\mathbf{u} + \nabla\mathbf{u}^T\right)\right]\cdot\mathbf{n}\; dA + \left(\hat{\rho}_p - \hat{\rho}_f\right)V_p\mathbf{g} + \mathbf{F}_c, \tag{3a}$$

$$\mathbf{T}_p = \oint_{\partial S_p}\mathbf{r}\times\left\{\left[-P\mathbf{I} + \hat{\mu}(\mathbf{u})\left(\nabla\mathbf{u} + \nabla\mathbf{u}^T\right)\right]\cdot\mathbf{n}\right\}\; dA + \mathbf{T}_c. \tag{3b}$$

In these equations ∂S_p represents the surface of the particles with outwards normal vector $\mathbf{n}$ and $\mathbf{I}$ the identity tensor, while $\mathbf{g}$ denotes the gravitational acceleration. The radial distance from the center to the surface of each particle is indicated by $\mathbf{r}$. The force and torque, $\mathbf{F}_c$ and $\mathbf{T}_c$, act on the particle as a result of particle-particle or particle-wall contacts. The no-slip and no-penetration boundary conditions on the surface of the particles are imposed by forcing the fluid velocity at each point on the surface of the particle, $\mathbf{X}$, to be equal to particle velocity at that point, $\mathbf{u}(\mathbf{X}) = \mathbf{U}^p(\mathbf{X}) = \mathbf{U}_c^p + \mathbf{\Omega}_c^p\times\mathbf{r}$. This condition is not imposed directly in the Immersed Boundary Method used in the current study, but instead included via the body force $\mathbf{f}$ on the right-hand side of Eq. (1).

2.1.1. Viscosity model

The Carreau model describes the inelastic behavior of fluids with shear dependent viscosity, so called pseudoplastic (shear-thinning) fluids such as polymeric solutions. This model describes the viscosity well-enough for most engineering calculations (Bird et al., 1987). The model presents an isotropic viscosity proportional to some power of the local deformation rate $\dot{\gamma}$ (Morrison, 2001),

$$\mu(\mathbf{u}) = \frac{\hat{\mu}_\infty}{\hat{\mu}_0} + \left(1 - \frac{\hat{\mu}_\infty}{\hat{\mu}_0}\right)\left[1 + (\lambda\dot{\gamma})^2\right]^{(n-1)/2}. \tag{4}$$

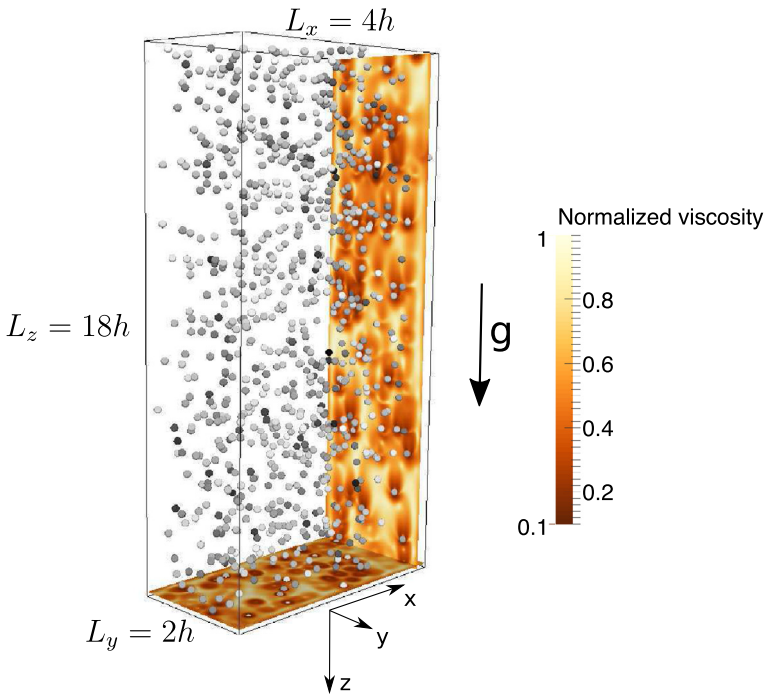

Fig. 1. Instantaneous visualisation of particle sedimentation for volume fraction $\Phi = 1\%$ through a shear thinning fluid bounded by two parallel walls. The contour plot shows the different normalized viscosity values on different wall-normal planes and the different settling velocities of particles from a lower (white) to higher (black) value. L_x, L_y and L_z represent the computational box size in the x, y and z directions; particle diameters are shown at their actual size.The particle diameter is equal to $2h/18$ with h the half channel width. The gravity is acting in the positive z direction. (For interpretation of the references to colour in this figure legend, the reader is referred to the web version of this article.)

In the expression above $\mu(\dot{\gamma})$ is the non-dimensional viscosity, normalized by $\hat{\mu}_0$, the zero shear-rate viscosity. $\hat{\mu}_\infty$ is the infinity shear rate viscosity and the ratio $\hat{\mu}_\infty/\hat{\mu}_0$ is set to 0.001 in our calculations. The second invariant of the strain-rate tensor, $\dot{\gamma}$, is determined by the dyadic product of the strain tensor, $\dot{\gamma} = (2\mathbf{G}:\mathbf{G})^{1/2}$ where $\mathbf{G} = \left(\nabla\mathbf{u} + \nabla\mathbf{u}^T\right)/2$ (see Ref. Bird et al., 1987). The power-index n indicates the non-Newtonian fluid behaviour: for $n < 1$ the fluid is shear-thinning and the fluid viscosity decreases monotonically with the shear-rate, while the viscosity becomes independent of the shear-rate (i.e. Newtonian fluid) when $n = 1$ and the non-dimensional viscosity takes the value $\mu = 1$. The material time constant, λ, is a dimensionless time scaled by the settling time scale and represents the degree of shear-thinning. In most of the current work, the time constant and the power-index are fixed to $\lambda = 10$ (Haque et al., 2012; Alghalibi et al., 2018) and $n = 0.6$, and only in the last section of the work we will evaluate the effect of changing λ. For a more detailed description of the parameters appearing in the Carreau model we refer the readers to Ref. Morrison (2001).

2.2. Numerical method

Several approaches have been proposed in recent years to perform interface-resolved Direct Numerical Simulations (DNS) of multiphase flows. In the present study, the gravity-driven motion of particles in a quiescent viscous fluid is simulated by means of an efficient immersed boundary method (IBM) coupled with a fluid phase solver for the generalised Navier-Stokes equations. The original IBM was developed by Uhlmann (2005) to fully resolve finite size particle suspensions and later on modified by Breugem (2012) to ensure second-order spatial accuracy. The fluid phase is computed by discretising the governing equations on a staggered mesh using a second order central difference scheme, where all the terms are treated explicitly. An equispaced ($\Delta x = \Delta y = \Delta z$) fixed and staggered Cartesian Eulerian mesh is used for the fluid phase whereas an uniform distribution of Lagrangian points is attached on the moving surface of each particle. The points of the Eulerian and Lagrangian grids communicate to calculate the IBM force which models the no-slip and no-penetration boundary conditions on the surface of the particles. The interactions between the particles or with a wall are taken into account using a lubrication correction and a soft collision model (Costa et al., 2015): when the thin gap distance between two approaching particles (or between particle and wall) becomes less than a certain threshold, lubrication correction models based on Brenner's asymptotic solution (Brenner, 1961) are employed to reproduce correctly the interaction between the particles; at smaller gaps the lubrication correction is kept constant to account for the surface roughness and, finally, a soft-sphere collision model is activated based on the relative velocity and the overlap between the particle-particle or particle-wall, where both the normal and tangential component of the contact force are taken into account. One issue concerns the use of the lubrication correction as suggested in the original IBM method of Breugem Breugem (2012) for Newtonian fluids in the case of shear-thinning fluids. To the best of our knowledge there is no good lubrication correction available for shear-thinning fluid and thus, we decided to rely on the analytical solution in Brenner (1961) anyway; to reduce its effect on the results, we limited the maximum volume fraction to 20% and to extend this model to shear-thinning fluids, we use in the asymptotic solution the local viscosity at the Eulerian point closest to the midpoint of the line connecting the centers of two particles in interaction, with the viscosity calculated explicitly from the local shear rate. For more details and validitions of the IBM code, the reader is referred to previous publications (Breugem, 2012; Lambert et al., 2013; Picano et al., 2015; Fornari et al., 2016; Lashgari

et al., 2016). Concerning the implementation of the viscosity model in the solver, we have tested the code for an unladen channel flow with shear-dependent viscosity fluid, and validated by comparing the result with the analytical solution (Nouar et al., 2007; Alghalibi et al., 2018).

2.3. Numerical setup

In this study the gravity-driven motion of solid spheres is examined in Newtonian and shear-thinning fluids bounded by parallel infinite flat walls located at $y = 0$ and $y = 2h$ with y the wall-normal direction. Periodic boundary conditions are imposed in the x and z directions, with gravity acting in the positive z direction. A zero volume flux is considered in the simulations. The computational box has size $L_x = 4h$, $L_y = 2h$ and $L_z = 8h$, where h is the half-channel width, see Fig. 1. The domain is discretised by a cubic mesh of 576 × 288 × 1152 points in the x, y and z directions. The ratio between the channel width, $H = 2h$, and the particle diameter, $2a$, is fixed to $h/a = 18$. The number of Eulerian grid points per particle diameter is 16 ($\Delta x = 1/16$) whereas 746 Lagrangian grid points are spread over the surface of each particle to resolve the fluid-particle interactions. In all our simulations, the time-step is chosen to ensure a CFL number equal to 0.75. The chosen time-step is sufficient to ensure the independence of the results on its value; we verified this by performing a simulation with a smaller value of the CFL number (0.2) and found that the difference in both the mean sedimentation velocity and its standard deviation is less than 0.2%.

Non-Brownian rigid spherical particles are considered with particle to fluid density ratio $\rho_p/\rho_f = 1.5$. The terminal settling velocity of the particles is not an input parameter to the simulations, as the non-dimensional parameter governing the particles sedimenting in a still fluid is the Archimedes number Ar (or the Galileo number $Ga = \sqrt{Ar}$). The Archimedes number quantifies the ratio between gravitational and viscous forces acting on the particle, defined as

$$Ar = \frac{\left(\frac{\rho_p}{\rho_f} - 1\right) g(2a)^3}{\hat{\nu}_0^2}, \tag{5}$$

where $\hat{\nu}_0$ is the zero shear-rate kinematic viscosity of the fluid. In the present work, the Archimedes number is kept constant to $Ar = 36$ for all shear-thinning fluid cases. Instead, for the simulations with a Newtonian fluid the Archimedes number is changed to $Ar = 97$ to reproduce almost the same terminal velocity of the single particle, V_t, calculated in the shear-thinning case (following the procedure explained in section §3.1).

In the current study we fix the rheological parameters as mentioned above and vary the solid volume fraction, Φ. Three different particle volume fractions, $\Phi = 1\%, 5\%$ and 20%, are chosen; these correspond to 891, 4455 and 17821 particles in the simulation domain. In all cases the particles are initialized randomly in the channel, with no overlap between each other, and with zero linear and angular velocities. A summary of the simulated cases is given in Table 1.

We display in Fig. 1 a snapshot of the spheres settling in shear-thinning fluid for $\Phi = 1\%$. The instantaneous normalised fluid viscosity values are shown on different wall-normal plans, while the settling velocity is indicated by the different colours used for the particles. The simulation results presented here are collected after the sedimentation reached a statistically steady state. In Fig. 2 we report the time history of the particles-averaged settling velocity, $\langle V_z \rangle_p(t)$, for one particular case ($\Phi = 5\%$, shear-thinning fluid). The settling velocity is normalised by the settling velocity of a single particle V_t whereas time is scaled by $(2a)/V_t$. The statistics are collected over the time interval indicated, after the initial transient

Table 1
Summary of the simulations performed. N_p indicates the total number of particles, D is the particle diameter while N_x, N_y and N_z are the number of grid cells in each direction. The lowest volume fraction corresponds to a single particle in the computational domain.

n	$\Phi(\%)$	N_p	Ar	$L_x \times L_y \times L_z$	$N_x \times N_y \times N_z$
0.6	1.12×10^{-5}	1	36	$36D \times 18D \times 72D$	$576 \times 288 \times 1152$
	1	891			
	5	4455			
	20	17821			
1	1.12×10^{-5}	1	97		
	1	891			
	5	4455			
	20	17821			

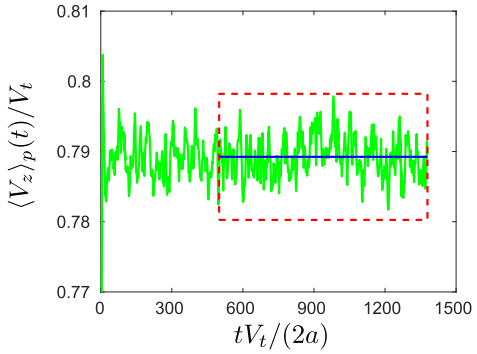

Fig. 2. Time history of the settling velocity, $\langle V_z \rangle_p(t)$, for one representative run ($\Phi = 5\%$, shear-thinning fluid). The settling velocity is normalised by the settling velocity of a single particle V_t, whereas time is scaled by $(2a)/V_t$. (For interpretation of the references to colour in this figure legend, the reader is referred to the web version of this article.)

phase. To ensure the results are statistically converged, we repeat the analysis using half the number of samples and compare the statistics with those from the entire number of samples: the difference between the two results is less than 1% for the first and second moments. The average of $V_{z,p}(t)$ over this statistically steady state is the mean settling velocity $\langle V_z \rangle_p$, indicated by the horizontal blue line, while the fluctuations are used to calculate the standard deviation of the settling velocity, $\sigma_{V_{z,p}}$. The $\langle . \rangle_p$ bracket denotes the average of a quantity over the total number of particles and time.

3. Results

In this work, we investigate and compare the behavior of sedimenting rigid particles in Newtonian (N) and shear-thinning (ST) fluids initially at rest. The results focus on the bulk properties of the suspension as well as its local behavior, e.g. particle settling and angular velocities, dispersions coefficients and particle local concentrations.

3.1. Sedimentation of an isolated particle

An isolated spherical particle settling in a quiescent shear-thinning fluid creates a local shear in the fluid surrounding it and the local viscosity seen by the particle decreases both around the particle and as a function of the distance from the particle surface Reynolds and Jones (1989) as shown in Fig. 1. This leads to a reduction of the drag on the particle Malhotra and Sharma (2012) and a consequent increase in the particle terminal velocity V_t, as compared to the settling in Newtonian fluid. Hence, to compare shear-thinning effects at the same values of V_t in the

Table 2
Central moments of the probability density functions of $V_{x,y,z,p}$ and $\omega_{x,y,x,p}$ normalized by the settling velocity of a single sphere V_t and $V_t/(2a)$ respectively. σ, S and K are the standard deviation, skewness and kurtosis of the probability density function. Note that for the spanwise rotation rate we compute $\tilde{\omega} = \langle \omega_x \cdot \text{sign}(y-h) \rangle_p$, as this is antisymmetric with respect to the centreline and that we do not report those quantities that should be zero across the channel by symmetry. (These attain values of the order $10^{-}3$, assessing the convergence of the statistics).

	N $\phi = 1\%$	ST $\phi = 1\%$	N $\phi = 5\%$	ST $\phi = 5\%$	N $\phi = 20\%$	ST $\phi = 20\%$
$\langle V_z \rangle_p / V_t$	0.8752	0.9644	0.6590	0.7887	0.3458	0.4677
$\sigma_{V_{z,p}}/V_t$	0.1586	0.1536	0.2541	0.2196	0.3336	0.3018
$\sigma_{V_{x,p}}/V_t$	0.0616	0.0539	0.1355	0.1055	0.1903	0.1967
$\sigma_{V_{y,p}}/V_t$	0.0545	0.0514	0.1242	0.1018	0.1742	0.1823
$S_{V_{z,p}}$	0.2728	1.0099	0.1153	0.2004	−0.1950	−0.1343
$K_{V_{z,p}}$	3.1027	4.5124	2.9902	2.9748	3.3978	3.0211
$\tilde{\omega}_p(2a)/V_t$	−0.0103	−0.0028	−0.0086	−0.0032	0.0038	0.0025
$\sigma_{\omega_{z,p}}(2a)/V_t$	0.0037	0.0038	0.0189	0.0189	0.0519	0.0709
$\sigma_{\omega_{x,p}}(2a)/V_t$	0.0610	0.0574	0.1360	0.1067	0.1937	0.2125
$\sigma_{\omega_{y,p}}(2a)/V_t$	0.0605	0.0546	0.1405	0.1094	0.1934	0.2162

different carrier fluids, we increase the Archimedes number, Ar, in the case of Newtonian fluid.

We start by performing two simulations of isolated particles settling in the same computational domain used for all studied cases (see Table 1), in both shear-thinning and Newtonian quiescent fluids. We determine the terminal settling velocity of the isolated sphere V_t in shear-thinning fluid and estimate the Archimedes number, Ar, that would reproduce the same value of the particle terminal velocity V_t in the Newtonian fluid. In particular, we have simulated the shear-thinning case with Archimedes number $Ar = 36$. By using the steady state settling velocity V_t, we define the terminal Reynolds number

$$Re_t = V_t(2a)/\hat{\nu}_0, \tag{6}$$

which in the present case is $Re_t = 3.89$. This can be related by empirical relations to the Archimedes number, Ar, of an isolated spherical particle settling in Newtonian quiescent fluid. Yin and Koch (2007), among others, used an empirical relation for the drag coefficient of a single particle as a function of Re_t when varying Ar, from which the relation between Ar and Re_t can be found (Fornari et al., 2016):

$$Ar = \begin{cases} 18Re_t\left[1 + 0.1315Re_t^{0.82-0.05log_{10}Re_t}\right], & 0.01 < Re_t \leq 20 \\ [2pt]18Re_t\left[1 + 0.1935Re_t^{0.6305}\right], & 20 < Re_t < 260 \end{cases} \tag{7}$$

The Archimedes number calculated from Eq. (7) is approximately 97 for $Re_t = 3.89$. We then perform the simulation of a single sphere setting in Newtonian fluid with $Ar = 97$ to check the validity of our approach. Indeed, the terminal Reynolds number Re_t, (or V_t), obtained with our simulation at $Ar = 97$ differs only by approximately 2% from the prediction using Eq. (7) ($Re_t = 3.81$, compared to the predicted value of 3.89).

3.2. Particle suspension: single-point particle statistics

In this section we investigate and compare the single-point particle statistics for the two studied cases, i.e. Newtonian and shear thinning carrier fluids, for different solid volume fractions $\Phi = [0.01, 0.05, 0.20]$. The single-point particle statistics are calculated by using quantities related to each individual particle, and taking a phase-ensemble average over time and space. In Table 2 we summarize the mean values extracted from these calculations. Note that for the spanwise rotation rate we compute $\langle \omega_x \cdot \text{sign}(y-h) \rangle_p$, as this is antisymmetric with respect to the centreline and that we do not report those quantities that should be zero across the channel by symmetry. These attain values of the order $10^{-}3$, assessing the convergence of the statistics. In addition, we also compute the mean and rms (linear and angular) velocities of the particles in the orthogonal directions (x, y, z) and the local particle volume fraction $\Phi(y)$, and velocities, as a function of the wall-normal coordinate y.

Independently of the suspending fluid and the particle concentration, the mean particle velocities in the spanwise and wall-normal directions, $\langle V_x \rangle_p$ and $\langle V_y \rangle_p$, are zero due to symmetry. In Fig. 3(a) we display the mean settling speed $\langle V_z \rangle_p$ as a function of the solid volume fraction Φ for the cases under investigation. The results are normalised by the corresponding terminal settling velocity V_t of an isolated particle in quiescent Newtonian and shear-thinning fluids. These are computed from the simulations of single particles discussed in the previous section §3.1. In all studied cases, the mean settling velocities are less than V_t and decrease monotonically by increasing the concentration of the dispersed phase as a consequence of the hindering effect (Nicolai et al., 1995; Yin and Koch, 2007; Guazzelli and Morris, 2011). The mean settling speed $\langle V_z \rangle_p$ is always larger in the shear thinning fluid than in the Newtonian one for the different volume fractions Φ investigated here. This is in agreement with the observations by Yu et al. (2006). The increase of $\langle V_z \rangle_p / V_t$ with respect to the Newtonian cases is 10.2%, 19.7% and 35.3% for $\Phi = 1\%$, 5% and 20%, respectively. We display the mean local fluid viscosity in the case of a quiescent shear-thinning fluid in Fig. 3(b); this decreases with the solid volume fraction Φ as a consequence of the increment of the local shear rate around the particles when the particle concentration Φ increases. To prove this, we consider the distribution of the local shear rate, quantified by the second invariant of the strain-rate tensor, $\dot{\gamma}_{local}(x, y, z)$, for all cases under investigation. In particular, Fig. 4 shows the probability density function (PDF) of $\dot{\gamma}^2_{local}(x, y, z)$ for all particle volume fractions Φ investigated in the present study, in the cases of Newtonian and shear-thinning suspending fluids. As expected, we observe that the range of shear rates increases significantly with the bulk concentration of the particles Φ and is always larger in the shear-thinning fluid than in the Newtonian one. In the shear-thinning fluid case, the increase of sampled shear rates ultimately leads to the reduction of viscosity reported in Fig. 3(b).

As mentioned before, the decrease of the mean viscosity of the fluid leads to a lower drag force acting on the particles and to an increase of the mean settling speed $\langle V_z \rangle_p$ with respect to the Newtonian cases. It is worth noting that, for a single particle there is a direct relation between the reduction of the viscosity and the increase in the terminal velocity. However, in a suspension particle-particle interactions play a role and a sort of collective behaviour can be observed preventing the velocity to linearly follow the change of viscosity. We believe this is due to the tendency of particles to fall side-by-side in a shear-thinning fluid as discussed

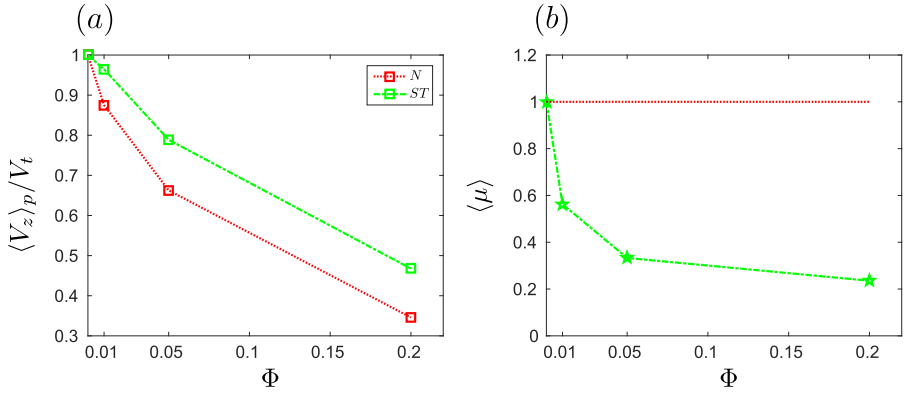

Fig. 3. (a) Normalised mean settling velocity, $\langle V_z \rangle_p / V_t$, and (b) non-dimensional mean fluid viscosity, $\langle \mu \rangle$, as a function of particle volume fraction Φ for both Newtonian, *N*, and shear-thinning, *ST*, cases. (For interpretation of the references to colour in this figure legend, the reader is referred to the web version of this article.)

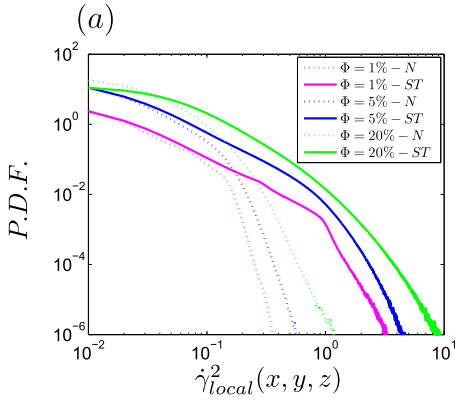

Fig. 4. Profiles of the probability density function (PDF) of the square of the local shear rate, $\dot{\gamma}^2_{local}(x,y,z)$, for all studied cases as indicated in the legend. (For interpretation of the references to colour in this figure legend, the reader is referred to the web version of this article.)

later in section §3.6, related to the hindrance effect when increasing particle concentration.

The particle velocity fluctuations along the *z* direction are depicted in Fig. 5(a) for all particle volume fractions Φ in the cases of Newtonian and shear-thinning fluids. The velocity fluctuations are scaled by V_t, see also Table 2. As shown in the figure, the standard deviations of the mean settling speed $\sigma_{V_{z,p}}$ changes slightly with the type of carrier fluids. The fluctuations increase with the volume fraction Φ and are lower in the shear-thinning fluid. The reduced level of fluctuations in the shear-thinning fluid is also associated to larger mean value of velocity, overall suggesting that particles feel approximately similar lower viscosity. On the other hand, the results show that independently of the type of suspending fluid, the particle velocity fluctuation $\sigma_{V_{z,p}}$ increases substantially with concentration (for Φ = 20%, $\sigma_{V_{z,p}}$ is nearly 2 times that found for Φ = 1%, in agreement with the experimntal observations by Nicolai et al. (1995) for a Newtonian fluid). Particles are closely packed and the dynamics is dominated by excluded volume effects, also in a shear-thinning fluid. This induces frequent particle-particle interactions, thus enhancing the velocity fluctuations. The ratio between the standard deviations in the direction perpendicular, $\sigma_{V_{j,p}}$, and parallel to the gravity, $\sigma_{V_{z,p}}$, which characterizes the anisotropy of the particle velocity fluctuations, is reported in Fig. 5(b), where $j = (x; y)$ indicates the coordinate directions. First, we observe that the fluctuations are always slightly lower in the *y*–direction than in the *x*–direction, $\sigma_{V_{y,p}}/\sigma_{V_{z,p}} < \sigma_{V_{x,p}}/\sigma_{V_{z,p}}$, due to the wall confinement effects. In the shear-thinning cases (ST) the ratio $\sigma_{V_{j,p}}/\sigma_{V_{z,p}}$ gradually increases with Φ up to Φ = 20%, while in the Newtonian case $\sigma_{V_{j,p}}/\sigma_{V_{z,p}}$ increases sharply up to Φ = 5% and then seems to saturate for higher volume fraction. It is also interesting to notice that the anisotropy is larger in the Newtonian fluid at lower Φ, whereas it is larger in the shear-thinning fluid at the highest volume fraction considered. At the lower Φ, the spheres fall faster, so tend to fall straight vertically with lower lateral fluctuations. However, at the highest volume fraction under investigation, the lateral fluctuations increase faster in the shear-thinning fluid than the deviation in the settling direction, indicating that the effect of viscosity reduction on the standard deviation of the particle distribution is not isotropic.

Next, we analyze the third and fourth moments of the velocity in the gravity direction, i.e. the skewness $S_{V_{z,p}}$ and kurtosis $K_{V_{z,p}}$. At low volume fractions Φ, the probability density function (PDF) of the settling velocity is positively skewed ($S_{V_{z,p}} > 0$) towards larger velocities than the mean settling velocity value. This is due to the fact that the most likely interactions (drafting-kissing-tumbling), taking place in the direction of gravity through the particle wakes, enhance the probability of having particles settling faster than the mean settling velocity $\langle V_z \rangle_p$ (therefore increasing the skewness). At larger volume fractions Φ, the excluded volume effects become more important than these specific particle-pair interactions, and the skewness $S_{V_{z,p}}$ reduces, eventually becoming negative at the largest volume fraction considered here due to the hindrance effect. Indeed, at large Φ the fluid moves in opposite direction to guarantee the balance of zero mixture velocity (Guazzelli and Morris, 2011) as will be explained later on, the probability of finding particles settling at lower speed than the mean increases, and hence the skewness becomes negative. In the shear-thinning cases, the skewness $S_{V_{z,p}}$ is always larger than in Newtonian fluid: this is due to the low viscosity in the particle surroundings which makes the nearby spheres fall with similar larger velocities, thus inducing overall larger skewness than in the Newtonian case. The kurtosis $K_{V_{z,p}}$ is approximately equal to 3 in the Newtonian case (similarly to a similar a Gaussian distribution) for all the volume fractions. On the other hand, the kurtosis is large (4.5) at low Φ in the shear-thinning fluid due to an increase of the intermittency of the drafting-kissing-tumbling events in shear thinning fluids (Fornari et al., 2016). $K_{V_{z,p}}$ slightly decreases with the volume fractions in the shear-thinning case, assuming a value approximately equal to the Newtonian case (≈ 3) at the largest Φ considered here.

All the previous results indicate that the particle dynamics are mostly dominated by collisions and particle-particle interactions and the properties of the fluid become less important once the macroscopic effect of change in the terminal velocity is suppressed.

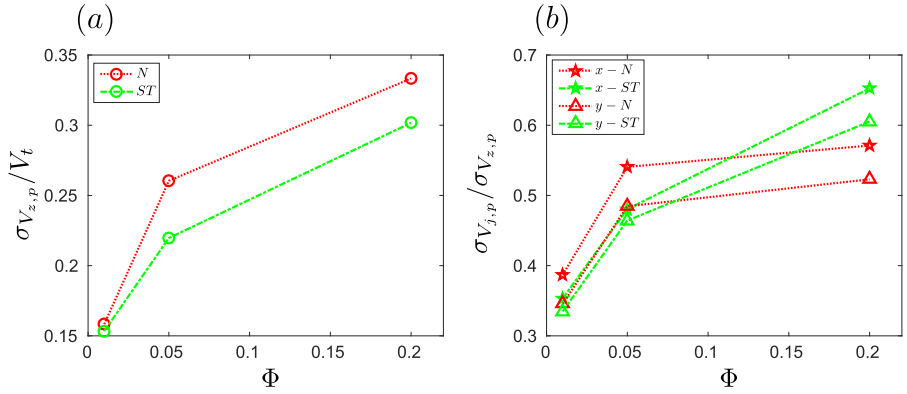

Fig. 5. (a) Standard deviations of the particle velocities parallel to gravity, $\sigma_{V_{z,p}}$ normalized by V_t. (b) Anisotropy of the particle velocity fluctuations, $\sigma_{V_{j,p}}/\sigma_{V_{z,p}}$, as a function of the particle volume fraction Φ for all cases investigated here. (For interpretation of the references to colour in this figure legend, the reader is referred to the web version of this article.)

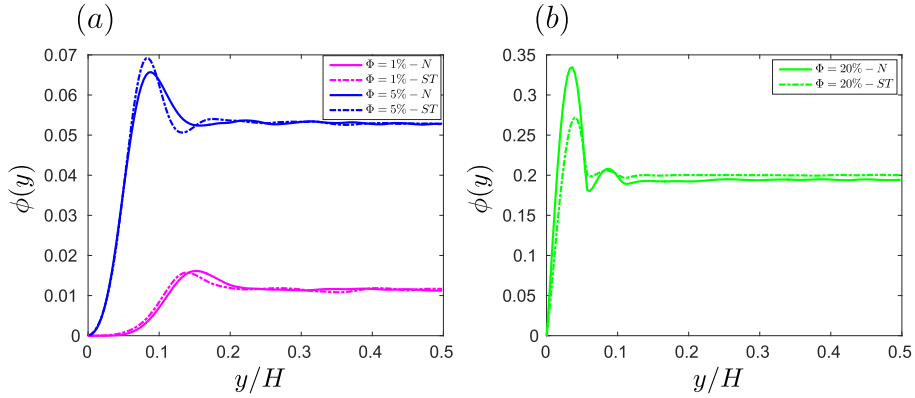

Fig. 6. The mean local volume fractions $\phi(y)$ versus the wall-normal coordinate y/H. (For interpretation of the references to colour in this figure legend, the reader is referred to the web version of this article.)

The main effect of the shear-thinning fluid in this case appears to be a reduction of particle interactions, resulting in reduced particle-velocity fluctuations.

3.3. Wall-normal profiles

We next analyse the particle behaviour across the channel. First, we display in Fig. 6(a,b) the wall-normal profiles of the mean local particle volume fraction, $\phi(y)$. The particle concentration is approximately constant in the middle of the channel and higher towards the walls due to the wall confinement. The peak of $\phi(y)$ moves toward the wall and grows as the bulk particle volume fraction, Φ, increases. At $\Phi = 0.01$, the maximum value of the mean local concentration is located around $y/H = 0.15$, a value slightly larger than 2.5 particle diameters ($H/2a = 18$), while it moves to $y/H = 0.035$, approximately at one particle radius from the walls for $\Phi = 0.2$. In particular, we observe in Fig. 6(a) that the distribution of $\phi(y)$ changes slightly with the carrier fluid for the two lowest volume fractions, $\Phi = [0.01, 0.05]$, suggesting that the local solid concentration is mainly controlled by confinement and geometry. However, panel 6(b), shows that the viscosity effects become clearer for the highest volume fraction under investigation ($\Phi = 0.2$), where the mean particle concentration in the intermediate region of the channel is 5% larger and the peak of $\phi(y)$ close to the wall is 18% smaller for the shear-thinning fluid. This is related to the wall-normal distribution of the fluid velocity in the settling direction $w(y)$, as will be shown later.

Secondly, we report the wall-normal profiles of the normalised mean settling velocity, $V_{z,p}(y)/V_t$, see Fig. 7(a). We observe that the spheres settle faster in the center of the channel than near the side walls in both carrier fluids at low particle concentrations $\Phi = [0.01, 0.05]$, suggesting that convection (so-called intrinsic convection) occurs in the channel in both the Newtonian and shear-thinning suspending fluids (Peysson and Guazzelli, 1998; Guazzelli and Morris, 2011). Interestingly, in the Newtonian case, the mean particle settling speed close to the wall is larger than that found in the center of the channel at the highest volume fraction under investigation ($\Phi = 0.2$), suggesting that the intrinsic convection occurs in the opposite direction. This inverse global convection is less evident in the ST case, and hence the variations of the mean settling velocity across the channel are different. It is also noteworthy to mention that, for all Φ, the settling velocities in a Newtonian suspending fluid are always smaller than those in a shear-thinning suspending fluid. This difference is mainly due to the local decrease of the fluid viscosity as discussed before.

Thirdly, we present in Fig. 7(b) the profiles of the mean spanwise particle angular velocities, $\langle \omega_x \cdot \mathrm{sign}(y-h) \rangle_p$, normalized by the settling velocity of a single particle and its diameter $V_t/(2a)$. As clear from the data, the spanwise particle rotation $\langle \omega_x \cdot \mathrm{sign}(y-h) \rangle_p$ is maximum close to the wall and tends to vanish toward the centre of the channel ($0.3 \leq y/H \leq 0.5$). At the highest volume fraction considered, the angular velocity is positive in the mid of the channel and changes sign just close to the wall, whereas it remains positive in the shear-thinning fluid. Moreover, for all the cases studied, $\langle \omega_x \cdot \mathrm{sign}(y-h) \rangle_p$ is lower in the shear-thinning fluid than in the Newtonian fluid near the wall.

To further confirm the intrinsic convection phenomenon mentioned above, we examine the statistics of the fluid-phase velocity. Figure 8 reports the wall-normal variations of the mean fluid ve-

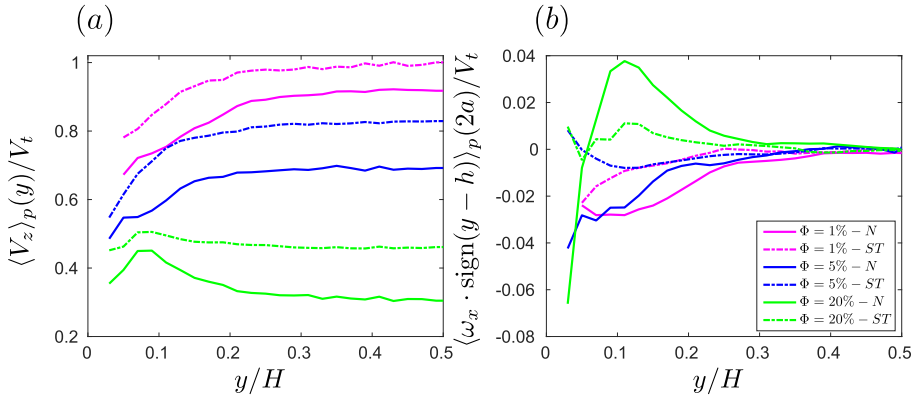

Fig. 7. Wall-normal profiles of the mean settling velocities $V_{z,p}(y)$ (left) and the absolute value of the mean particle angular velocities, $\langle \omega_x \cdot \mathrm{sign}(y-h) \rangle_p$ (right), normalized by the settling velocity of a single sphere V_t and $V_t/(2a)$ respectively, for all studied cases as indicated in the legend. (For interpretation of the references to colour in this figure legend, the reader is referred to the web version of this article.)

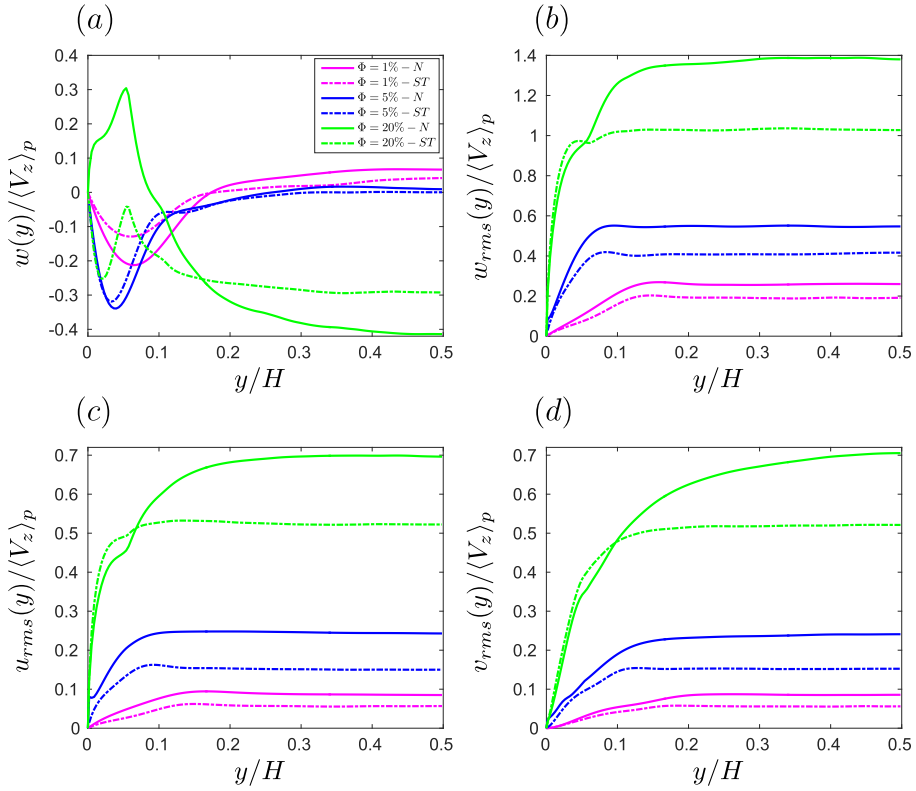

Fig. 8. Wall-normal profiles of the mean fluid velocities in the settling direction, $w(y)$ and the fluctuation of the fluid velocity components in the three directions for all the studied cases. The data are normalized by the mean settling velocity, $\langle V_z \rangle_p$. (For interpretation of the references to colour in this figure legend, the reader is referred to the web version of this article.)

locity in the settling direction and the root-mean-square (r.m.s.) of the fluid velocity fluctuations in the three directions, normalized by their mean settling velocity, $\langle V_z \rangle_p$. The statistics pertaining the fluid-phase velocity have been calculated neglecting the points located inside the volume occupied by the solid phase in each field (phase-ensemble average).

At the lower particle concentrations, $\Phi = [0.01, 0.05]$, we see in Fig. 8(a) the formation of an upward flow (negative velocity is opposite to gravity) in the particle-depleted layer close to the wall. This tends to pull the bulk of the particle suspension up and hence reduces the mean particle settling velocity, as mentioned previously when discussing Fig. 7(a). It is interesting to notice that the maximum of the normalized upward mean local fluid velocity is higher in the Newtonian fluid than in the shear-thinning fluid and its location moves towards the wall with increasing particle concentration. At $\Phi = 0.01$, the near wall velocity peak reaches a value of $w_{\max} \approx -0.2\langle V_z \rangle_p$ at a distance from the wall slightly larger than one particle diameter ($y/H \approx 0.064$) in the Newtonian case, while in the case of the shear-thinning fluid, $w_{\max}$ decreases to approximately $-0.13\langle V_z \rangle_p$. When increasing the bulk volume fraction to $\Phi = 0.05$, $w_{\max}$ grows to $-0.4\langle V_z \rangle_p$ at $y/H \approx 0.036 = 0.65(2a)$ in the Newtonian fluid and to $-0.33\langle V_z \rangle_p$ in the shear-thinning fluid. In the latter case, the decrease of the drag force acting on the settling particles, due to the reduction of the mean local fluid viscosity seen by them, leads to a decrease of the upward mean local fluid velocity.

In the case of particles sedimenting in a wall-bounded fluid, the fluid flow is approximately parallel to the settling direction with

zero net flow in the horizontal directions Bruneau et al. (1996); Guazzelli and Morris (2011). To satisfy this condition, a small inverse pressure gradient is required to drive a return flow in the positive z direction in the middle of the channel, as shown in Fig. 8(a) at the lower particle concentrations ($\Phi = 0.01, 0.05$). This produces fluid flow on each half of the channel with ascending (negative z) fluid velocity near the wall and descending (positive z) in the center; this leads to the intrinsic convection, by which the settling particles and the fluid move together in the middle region and the particles fall faster in the center of the channel than near the walls.

However, as the particle concentration is further increased ($\Phi = 0.2$), due to the high local concentration of the particle near the side walls and the no-slip boundary condition, the spheres drag the fluid with them in the settling direction. So the fluid velocity is positive with a maximum value reaching $w_{\max} = 0.3\langle V_z\rangle_p$ at approximately one particle diameter from the wall ($y/H \approx 0.054$). The circulation is completed by an upward return flux in the middle of the channel with a maximum speed of about $-0.42\langle V_z\rangle_p$, indicating a reversal of the global intrinsic convection at $\Phi = 0.2$. This opposite global convection contributes to increase the hindrance effect and therefore, the particles fall slower in the center than near the walls at high volume fractions, see Fig. 7(a).

It is also noteworthy to mention that, due to the large difference between the mean fluid speed in the center of the channel and near the walls for high Φ, a strong opposite flow is formed with an ascending fluid velocity in the center and descending fluid close to the walls. This pushes more particles into the layer near the wall and therefore promotes an increase of the local particle concentration $\Phi(y)$ close the wall, as shown in Fig. 6(b) for the Newtonian case. Unlike the Newtonian case, the global convection is less evident for the shear-thinning case at the same Φ, as shown by the distribution of the mean local fluid velocity $w(y)$ across the channel. The fluid moves upwards in two regions (nearby the wall and in the center of the channel) with maximum velocities approximately $-0.25\langle V_z\rangle_p$ and $-0.27\langle V_z\rangle_p$, and the circulations are completed by a downward return flow around one sphere diameter from the wall ($y/H \approx 0.055$). This suggests that, two opposite flows are forming on each channel half, which leads to a decrease of the intrinsic convection of the suspension and hence to different wall-normal profiles of the particle settling speeds, as revealed in Fig. 7(a).

As regards the r.m.s of the fluid velocity field, see Fig. 8(b-d), these are approximately constant in the middle of the channel and sharply decrease near the side walls. Nevertheless, a difference due to the shear-thinning effects is evident, as the fluctuations are always smaller in the shear-thinning cases. Furthermore, regardless of the type of carrier fluid, the fluctuations of the velocity are approximately 50% larger in the direction parallel to gravity due to the long-range disturbance induced by the sphere wakes. Finally, the increase of particle concentration Φ enhances the r.m.s. of the velocity fluctuations in all directions, suggesting that the dynamics is mainly determined by excluded volume effects in both phases. It is worth noting that, the fluctuations in the fluid velocity are related to the particle velocity fluctuations, hence smaller fluid velocity fluctuations in the shear-thinning case are in line with the already observed (see Table 2) smaller particle velocity fluctuations.

3.4. Particle velocity correlations

To further understand the effect of a shear-dependent fluid viscosity on the sedimentation of spherical particles, we examine the two-time correlations of the particle velocity fluctuations. In this study, the autocorrelation function is calculated only in the x and z directions; the autocorrelation of the particle velocity fluctuations as a function of the temporal separation, τ is defined as follows (Fornari et al., 2016):

$$R_{V_iV_i}(\tau) = \frac{\langle V'_{i,p}(p,t)V'_{i,p}(p,t+\tau)\rangle}{\sigma^2_{V_{i,p}}}. \tag{8}$$

$R_{V_iV_i}(\tau)$ is often used to define an integral timescale, T_i:

$$T_i = \int_0^\infty R_{V_iV_i}(\tau)\, d\tau, \tag{9}$$

where $i = (x, z)$ is the coordinate directions and $V'_{i,p}(p,t) = V_i(p,t) - \langle V_i\rangle_p$ is the fluctuation velocity with respect to the mean velocity over the particle ensemble and time (for more details, the reader is referred to Ref. Uhlmann and Doychev, 2014); note that $\langle V_x\rangle_p$ is equal to 0. T_i gives an estimate of the time interval over which the particle velocity fluctuation component is correlated.

Fig. 9 (a) and (b) show the autocorrelations $R_{V_zV_z}$ and $R_{V_xV_x}$, for both Newtonian and shear-thinning fluids, as a function of the normalized time τ. For all the cases, as expected, the particle velocity autocorrelation decreases towards zero, which confirms that the particle velocities become uncorrelated for large τ. Moreover, as a general trend, the decay of the correlation functions is always faster in the shear-thinning fluid than in the Newtonian one at the same volume fractions Φ. To better highlight these differences, we provide in panel (c), the values of the correlation times; the correlation time strongly decreases from $\Phi = 1\%$ to 5%, while for the largest Φ it remains approximately constant for the Newtonian fluid and only slightly decreases for the shear-thinning one. Also, the correlation time is always larger in the Newtonian cases than in the shear-thinning cases.

3.5. Particle dispersions or hydrodynamic self-diffusion

To further focus on the particle dynamics, we study the single-particle dispersion, i.e., the mean square displacement, for both type of fluids at various volume fractions. The long time uncorrelated particle velocity fluctuations induce a chaotic transport of the settling particles across the channel. This overall stochastic motion is generally called hydrodynamic self-diffusion or particle dispersion. The particle dispersion dynamics are most conveniently captured by studying the particle lateral displacement, which results from hydrodynamic and particle-particle interactions. The dispersion is measured by the variance of the displacement of the particle as function of the temporal separation, τ. We examine only the single-point mean-square displacement of particles in the x direction, i.e., $\langle \Delta x_p^2\rangle$. Here, the mean square displacement of the particle trajectories is defined by

$$\left\langle \Delta x_p^2(\tau)\right\rangle = \langle [x_p(t+\tau) - x_p(t)]^2\rangle_{p,t}, \tag{10}$$

where x_p is the vector containing the x position of the particle centres, τ is the time interval and $\langle . \rangle_{p,t}$ denotes averaging over all times, t, and particles, p. The particle diffusion coefficients in the x direction, D_{xx} can then be computed by calculating the half of the slope of the linear part (for large values of τ) of the single-point mean-square displacement,

$$D_{xx} = \frac{\langle \Delta x_p^2(\tau)\rangle}{2\tau}. \tag{11}$$

For more details about this topic we refer the readers to previous works, see e.g. Refs. Da Cunha and Hinch (1996), Sierou and Brady (2004), Janoschek (2013) and Lashgari et al. (2016).

Fig. 10 (a) shows the particle mean square displacement, $\langle \Delta x_p^2\rangle$, as a function of the normalised time, $\tau V_t/(2a)$ while the diffusion coefficient, D_{xx}, is reported in panel (b) of the same figure versus the particle concentrations Φ. Note that the mean square displacement, $\langle \Delta x_p^2\rangle$, is normalised by $(2a)^2$ whereas the diffusion

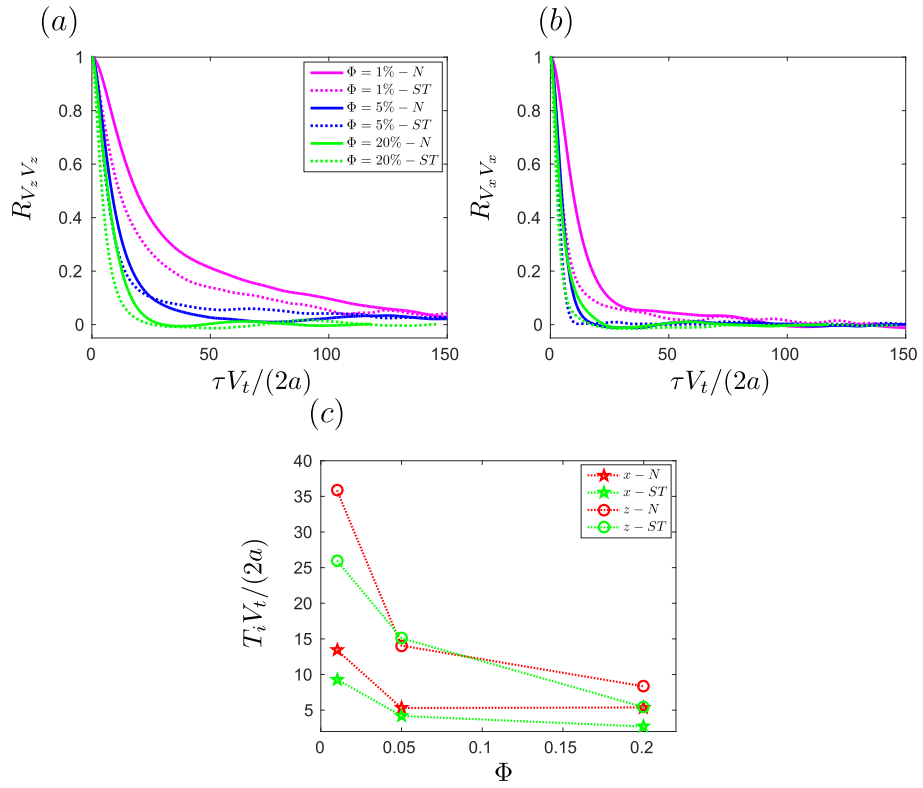

Fig. 9. (top) Time correlation profiles and (bottom) correlation time of the particle velocity fluctuation components for the different cases under consideration. (For interpretation of the references to colour in this figure legend, the reader is referred to the web version of this article.)

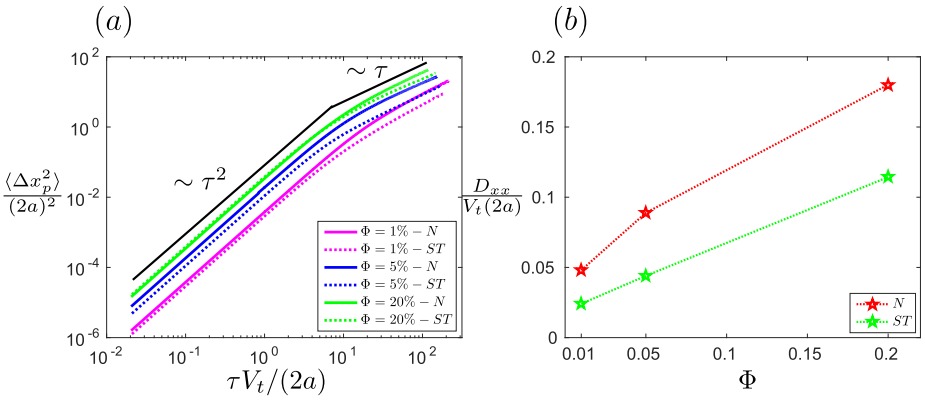

Fig. 10. (left) Profiles of the time evolution of the normalised mean square particle displacement along particle trajectories in the x direction for the all cases under investigation and (right) the correspondent mean-square displacement. (For interpretation of the references to colour in this figure legend, the reader is referred to the web version of this article.)

coefficient, D_{xx}, is expressed in units of $V_t(2a)$. For all the cases, as expected, the particle trajectories are initially highly correlated at small intervals and the mean-square dispersion profiles varies quadratically in time, $\langle \Delta x_p^2(\tau) \rangle \propto \tau^2$. Later on, after $\tau \sim 10(2a)/V_t$, the classical diffusive behaviour takes over: the particle trajectories decorrelate due to the particle-particle and hydrodynamic interactions and the mean square displacement varies linearly with time, $\langle \Delta x_p^2(\tau) \rangle \sim 2D_{xx}\tau$.

The behaviour of the two fluids is quite similar, so to better highlight the differences we provide in Fig. 10(b), the normalised value of the particle self-diffusion coefficient, D_{xx}, computed as half the slope of the linear growth rate of the particle mean-square displacement $\langle \Delta x_p^2 \rangle$. Clearly, the results show that, the particle diffusion coefficient D_{xx} is strongly dependent on the particle volume fraction Φ; in particular, D_{xx} increases monotonically with Φ as a consequence of the increasing hydrodynamic and particle-particle interactions. Furthermore, we observe that in the shear-thinning fluid, the diffusion coefficient is always smaller than in the Newtonian case by abound 50%, which we can relate to the reduced velocity fluctuations previously observed in the shear-thinning fluid.

3.6. Particle-pair statistics

In this last section, we consider particle-pair statistics as a function of the distance between the centres of the particle pairs, r, to investigate the microstructure of the entire suspension. In particular, we study the pair probability distribution function, $P(\mathbf{r})$, which is used to describe how, on average, the spheres are radially packed around each other and to measure the level of anisotropy in the particle suspensions Sierou (2002); Kulkarni and

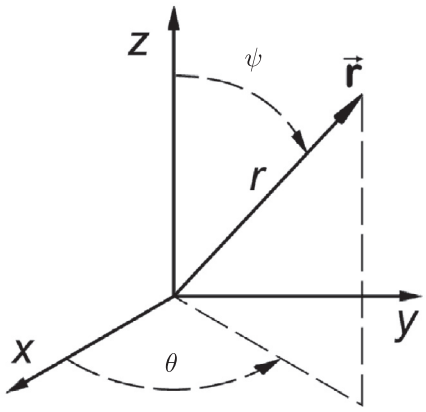

Fig. 11. Definitions of the polar angle ψ and the azimuthal angle θ in Cartesian coordinates.

Morris (2008). Mathematically, following Refs. Kulkarni and Morris (2008) and Fornari et al. (2018), the pair distribution function in a spherical coordinate system is defined by

$$P(\mathbf{r}) = P(r, \theta, \psi) = \frac{N(r, \psi, \theta)}{t_s n_0 \Delta Q_s}, \tag{12}$$

where ψ is the polar angle (measured from the positive z axis), θ is the azimuthal angle (measured from the positive x axis) as shown in Fig. 11, t_s is the total number of sampling points, $N(r, \psi, \theta)$ is the histogram of particle pairs that lie within a sampling bin shell element with a nominal radius r and a radial width Δr, $\Delta Q_s = r^2 \Delta r \sin\psi \Delta\theta \Delta\psi$ is the volume of the sampling bin shell and $n_0 = 0.5 N_p (N_p - 1)/Q$ is the averaged particle pairs density in the total volume Q, with N_p the total number of particles. In our configuration, the flow is asymmetric in the gravity direction. Nevertheless, the pair distribution function is symmetric in the gravity direction. This observable measures the relative position of particle pairs, so one particle below the reference particle would correspond to one above when this becomes the reference in the statistics. We thus report $P(\mathbf{r})$ as a function of two variables: the center-to-center distance r (normalized by the diameter 2a), and the polar angle ψ, averaging over the angle θ.

Fig. 12 (a-d) shows the pair distribution function $P(\mathbf{r})$ for the lowest (a,b) and highest (c,d) volume fractions Φ in the cases of Newtonian (a,c) and shear-thinning (b,d) fluids. Exploiting the symmetry discussed above, the function is displayed only in the range $\psi \, in [0, \pi/2]$. In the Newtonian case (left column), we observe that, at low volume fraction, the particles tend to be far apart, with a local peak of $P(\mathbf{r})$ for $\psi = 0$ and $r \approx 6a$. As the volume fraction increases, the particles mean distance reduces and its distribution becomes more uniform in the polar direction ψ. In the shear-thinning case, the situation is similar at high volume fraction, where the effect of the packing is dominant, whereas differences are evident in the more dilute regimes. In particular, we note that particles tend to be on average close than in the Newtonian case, with strong peaks of $P(\mathbf{r})$ both along $\psi = 0$ and $\pi/2$. This indicates that particles tend to form aggregates in a shear-thinning fluid, preferentially positioning in the wake of neighboring particles or beside them, thus resulting in lower levels of fluctuation in the gravity direction than in the Newtonian fluid as discussed above. This also suggests that in quiescent Newtonian fluid, particles have a mean horizontal spacing of 6 radii. Now it is interesting to note that in shear thinning fluids, the pair distribution function increases not only in the gravity direction. Generally above the reference particle, we see a clear increase of $P(\mathbf{r})$ above the reference

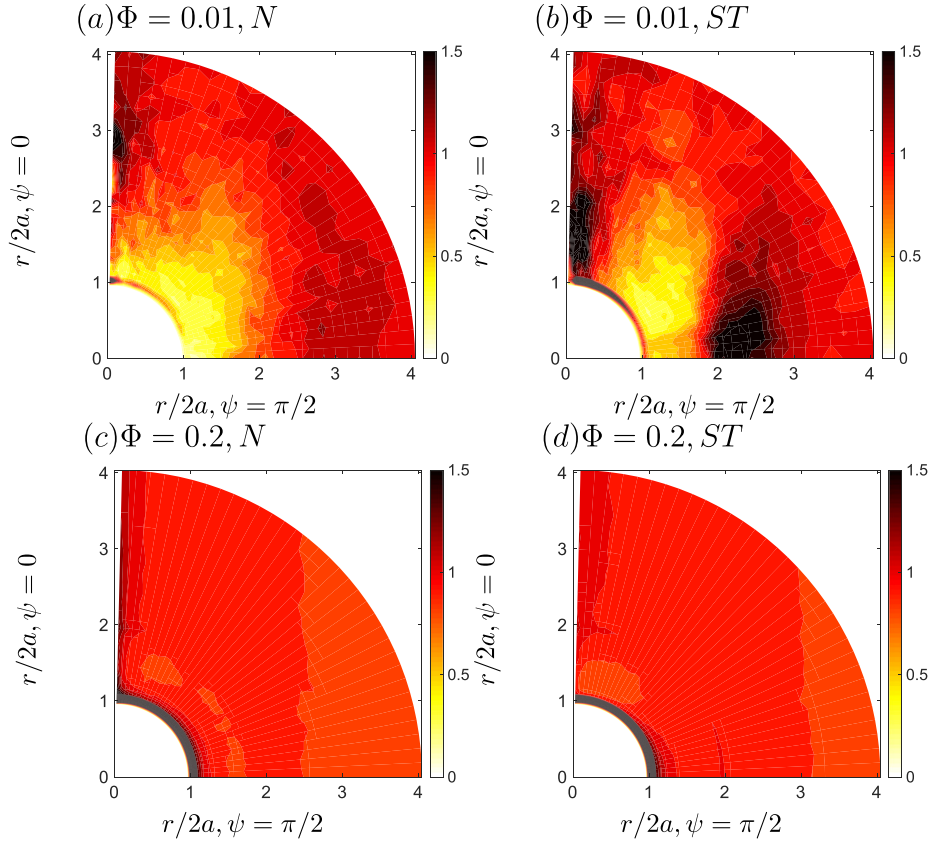

Fig. 12. Pair-distribution function $P(r, \psi)$ for the lowest and highest volume fractions considered, $\Phi = 0.01$ and 0.2, respectively. The left and right columns are used for the Newtonian and shear-thinning fluids. (For interpretation of the references to colour in this figure legend, the reader is referred to the web version of this article.)

Table 3
Summary of the simulations performed at the same Archimedes number.

n	λ	$\Phi(\%)$	N_p	Ar	$L_x \times L_y \times L_z$	$N_x \times N_y \times N_z$
0.6	10,20,40	1	891	36	$36D \times 18D \times 72D$	$576 \times 288 \times 1152$
1	0	1	891	36		

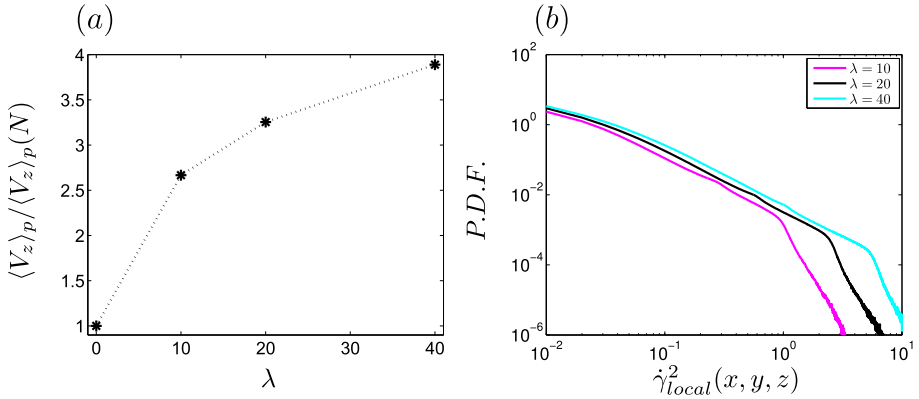

Fig. 13. (a) Normalised mean settling velocity, $\langle V_z \rangle_p / \langle V_z \rangle_p(N)$, and (b) probability density function (PDF) of the local shear rate, $\dot{\gamma}^2_{local}(x, y, z)$, as a function of the shear-thinning time scale λ at the same volume fraction $\Phi = 1\%$ and Archimedes number $Ar = 36$. (For interpretation of the references to colour in this figure legend, the reader is referred to the web version of this article.)

particle. The extent of clustering increases due to shear thinning in the particle surrounding that leads to stronger drafting-kissing-tumbling effects/interactions, with the kissing phase lasting longer. At the same time, the smaller viscosity around the reference particle induces a small scale lateral migration of neighboring particles which approach the reference one; indeed, the peak values of $P(\mathbf{r})$ for $\psi = \pi/2$ move from $6a$ in the Newtonian fluid to around $4.5a$ in the shear-thinning one. In addition, the effect is strong and the maximum value of $P(\mathbf{r})$ at this location increases with respect to the Newtonian case. It is therefore highly probable to find particles falling side-by-side, at a distance of around $4 - 5a$.

3.7. The effect of the shear-thinning fluid on suspensions at the same Archimedes number.

Finally, in this last section we study the effect of the shear-thinning time scale λ. The volume fraction of the particles Φ is now fixed to 0.01 to better highlight the effect of the shear-thinning fluid and reduce that of the particle packing. Furthermore, we fix the Archimedes number, which results different terminal velocities, in order to evaluate the total effect of the shear-thinning fluid on the suspensions. The studied cases are reported in Table 3.

First, Fig. 13a reports the normalised mean settling velocity $\langle V_z \rangle_p$ as a function of the shear-thinning time scale λ. We observe that the terminal velocity monotonically increases with λ and is thus always larger in the shear-thinning fluid than in the Newtonian one. This is consistent with what previously observed in the case of isolated particles Malhotra and Sharma (2012). The increase of sedimentation velocity is due to the modification of the local viscosity around the particles; indeed, as reported in Fig. 13b, the local shear rate increases with the level of shear-thinning λ, resulting in a reduced particle drag due to smaller values of local viscosity.

Next, we report in Fig. 14 the pair-distribution function $P(r, \psi)$ for different values of λ. Although the overall behaviour is similar to what previously discussed, we now clearly observe that as the shear-thinning effect increases the peak of P located at around $r \approx 4a$ progressively reduces, indicating a more uniform distribution of particles for large values of λ.

The results presented in this section and those previously reported are complementary: in the previous sections we were considering cases with the same terminal velocity in the single particle case and different Archimedes numbers, while now cases with the same Archimedes number and different terminal velocities in the single particle case. These two results together indicate that the shear-thinning effect on the particle sedimentation is indeed twofold: first, it modifies the particle sedimentation velocity due to changes in the fluid viscosity; secondly, it modifies the level of particle interactions.

4. Conclusion and remarks

We performed a series of simulations to study the settling behavior of finite-size heavy particles at finite terminal Reynolds number Re_t in shear-thinning and Newtonian quiescent fluids in a vertical channel. The problem is studied through direct numerical simulations based on an efficient direct-forcing immersed boundary method to capture the fluid-structure interactions. The Carreau model is employed to describe the rheological behavior of the shear-thinning carrier fluid, where the fluid viscosity varies instantaneously with the local fluid shear rate, $\dot{\gamma}$. We consider a suspension of monodisperse rigid spheres with fixed ratio between the particle diameter and channel width equal to 1/18 and vary the total volume fraction of the solid phase in the range $1 \leq \Phi \leq 20\%$. In the first set of simulations, the Archimedes number is set to $Ar = 36$ for the shear-thinning fluid while it is increased to $Ar = 97$ for the Newtonian case to obtain almost the same value for the settling velocity of an isolated particle (same Re_t) as in the shear-thinning case. By doing so, we aim to remove the first-order effect of the difference between the two fluids (a different mean viscosity) and maintain only those due to particle-particle interactions and viscosity fluctuations. In this way, we find that, when the macroscopic effect of the change in sedimentation velocity is suppressed, the effect of shear-thinning is rather limited.

We show that the mean settling velocity of a suspension decreases with the volume fraction and increase in the shear-thinning fluid. This is the result of the competition between two opposite effects, related to different physical mechanisms: i) the hindrance effect, which reduces the mean settling velocity

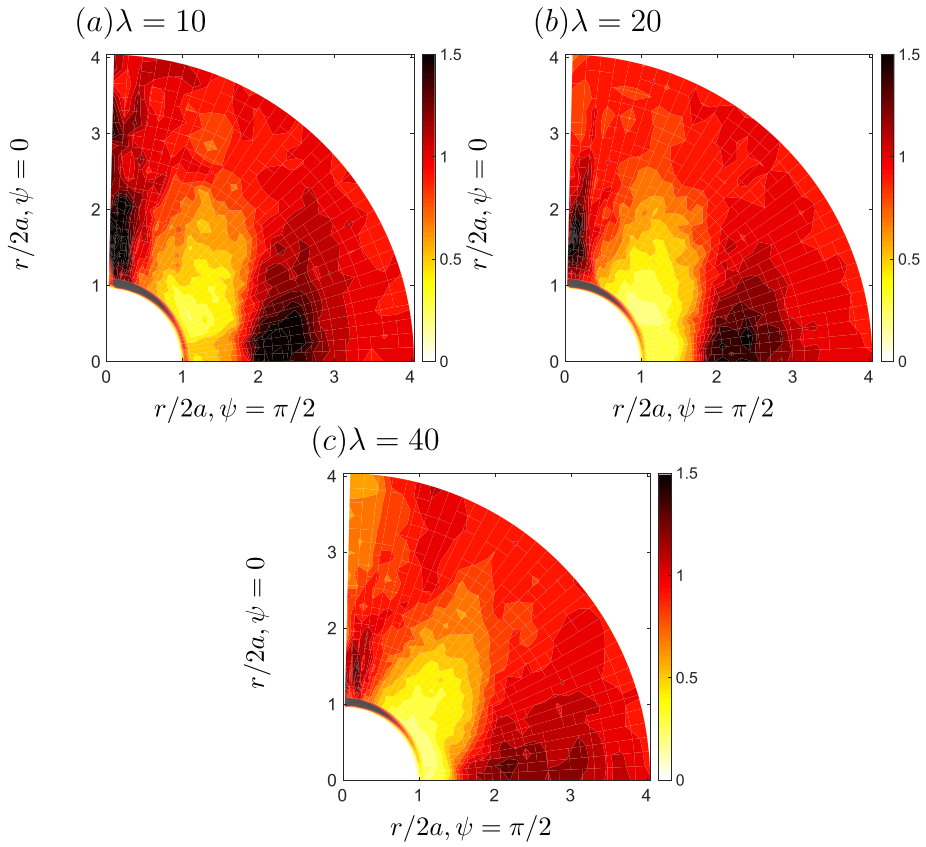

Fig. 14. Pair-distribution function $P(r, \psi)$ for different values of λ at a fixed volume fraction $\Phi = 1\%$ and Archimedes number $Ar = 36$. (For interpretation of the references to colour in this figure legend, the reader is referred to the web version of this article.)

and monotonically increases with Φ; ii) the shear-thinning effect, which also increases with Φ as a consequence of the reduction of the local shear rate and, as a consequence, of the fluid viscosity around the particles and leads to an increase of the mean settling velocity. The velocity fluctuations in the gravity direction increase substantially with the solid volume fraction in both fluids but is lower in the shear-thinning fluid than in the Newtonian one. From the probability density function of the settling velocity, we find a high probability of particles settling faster than the mean settling velocity at low concentrations, while the opposite trend is observed at high volume fractions. This effect is present in both fluids, but it is strengthened in the shear-thinning fluid. We also find a large value of the fourth-order moment in the shear-thinning fluid, indicating a highly intermittent behavior at low volume fractions, which eventually vanishes for higher concentrations.

The local profile of the solid volume fractions revealed the formation of particle layers close to the walls for all cases. The distribution of particles settling across the channel is mainly controlled by geometry and confinement effects, with a weaker dependency on the type of suspending fluid. We find that intrinsic convection occurs through the channel in both carrier fluids at low Φ, which induces an increase of the particles settling velocity in the channel center. On the contrary, this convection is reversed at the highest volume fraction investigated, especially in the Newtonian fluid. The particle lateral dispersion strongly depends on the concentration of the particles and it is always lower in a shear-thinning fluid than in a Newtonian one.

We computed the pair distribution functions to study the microstructure of the suspensions, and demonstrated that in both fluids an almost uniform distribution is present at high volume fraction Φ due to the reduction of the particles mean distance and the high packing. On the other hand, the pair distribution functions clearly shows the tendency to form aggregates in a shear-thinning fluid, with particles preferentially positioning in the wake or beside each other, which overall results in lower levels of velocity fluctuations in the gravity direction than in a Newtonian fluid.

Finally, we studied the effect of the shear-thinning time scale λ on the particle sedimentation. In this case we fix the Archimedes number Ar and let the terminal velocity vary freely. As expected, we find that the terminal velocity strongly increases with the level of shear-thinning, up to a factor 4 in the range of parameters investigated. The progressive raise in terminal velocity with λ is related to the reduction in the viscosity caused by increasing shear rates with λ.

Overall, we find a twofold effect of shear thinning on the particle sedimentation. First, the macroscopic effect of the shear-thinning carrier fluid is the substantial modification of the particle sedimentation velocity, which is always larger in the shear-thinning case than in the Newtonian one. This is mainly due to increase of shear rates around the particles accompanied by changes in the local viscosity leading to a reduced particle drag. Secondly, the shear-thinning fluid reduces the level of particle interactions, causing a reduction of velocity fluctuations resulting in particles sedimenting together at approximately the same speed.

With this study we have evaluated the role of shear thinning on the sedimentation of a suspension of inertial particles. Future works should extend the analysis to more complex non-Newtonian fluids, taking into account for example elasticity and yield stress.

Declaration of Competing Interest

The authors declare that they have no known competing financial interests or personal relationships that could have appeared to influence the work reported in this paper.

CRediT authorship contribution statement

Dhiya Alghalibi: Formal analysis, Investigation, Data curation, Writing - original draft, Visualization, Writing - review & editing. **Walter Fornari:** Methodology, Formal analysis, Investigation, Data curation, Writing - review & editing. **Marco E. Rosti:** Formal analysis, Investigation, Data curation, Writing - review & editing. **Luca Brandt:** Conceptualization, Resources, Writing - review & editing, Supervision.

Acknowledgments

LB was supported by the European Research Council Grant no. ERC-2013-CoG-616186, TRITOS and by the Swedish Research Council Grant no. VR 2014-5001. DA would like to gratefully acknowledge his graduate scholarship from the Iraqi Ministry of Higher Education and Scientific Research via University of Kufa. The authors acknowledge computer time provided by the Swedish National Infrastructure for Computing (SNIC).

Supplementary material

Supplementary material associated with this article can be found, in the online version, at 10.1016/j.ijmultiphaseflow.2020.103291 .

References

Alghalibi, D., Lashgari, I., Brandt, L., Hormozi, S., 2018. Interface-resolved simulations of particle suspensions in Newtonian, shear thinning and shear thickening carrier fluids. J. Fluid Mech. 852, 329–357.
Allen, E., Uhlherr, P., 1989. Nonhomogeneous sedimentation in viscoelastic fluids. J. Rheol. 33 (4), 627–638.
Becker, L., McKinley, G., Stone, H., 1996. Sedimentation of a sphere near a plane wall: weak non-Newtonian and inertial effects. J. Nonnewton Fluid Mech. 63 (2–3), 201–233.
Bird, R.B., Armstrong, R.C., Hassanger, O., 1987. Dynamics of Polymeric Liquids, vol. 1, second ed. Wiley-Interscience.
Bobroff, S., Phillips, R.J., 1998. Nuclear magnetic resonance imaging investigation of sedimentation of concentrated suspensions in non-Newtonian fluids. J. Rheol. 42 (6), 1419–1436.
Brenner, H., 1961. The slow motion of a sphere through a viscous fluid towards a plane surface. Chem. Eng. Sci. 16 (3), 242–251.
Breugem, W.-P., 2012. A second-order accurate immersed boundary method for fully resolved simulations of particle-laden flows. J. Comput. Phys. 231, 4469–4498.
Bruneau, D., Feuillebois, F., Anthore, R., Hinch, E.J., 1996. Intrinsic convection in a settling suspension. Phys. Fluids 8 (8), 2236–2238.
Chhabra, R.P., 2006. Bubbles, Drops, and Particles in Non-Newtonian Fluids. CRC press.
Clift, R., Grace, J.R., Weber, M.E., 2005. Bubbles, Drops, and Particles. Courier Corporation.
Climent, E., Maxey, M., 2003. Numerical simulations of random suspensions at finite Reynolds numbers. Int. J. Multiph. Flow 29 (4), 579–601.
Costa, P., Boersma, B.J., Westerweel, J., Breugem, W.-P., 2015. Collision model for fully resolved simulations of flows laden with finite-size particles. Phys. Rev. E 92, 53012.
Da Cunha, F., Hinch, E.J., 1996. Shear-induced dispersion in a dilute suspension of rough spheres. J. Fluid Mech. 309, 211–223.
Daugan, S., Talini, L., Herzhaft, B., Peysson, Y., Allain, C., 2004. Sedimentation of suspensions in shear-thinning fluids. Oil Gas Sci. Technol. 59 (1), 71–80.
Davis, R.H., Acrivos, A., 1985. Sedimentation of noncolloidal particles at low Reynolds numbers. Annu. Rev. Fluid Mech. 17 (1), 91–118.
Di Felice, R., 1999. The sedimentation velocity of dilute suspensions of nearly monosized spheres. Int. J. Multiph. Flow 25 (4), 559–574.
Fornari, W., Ardekani, M.N., Brandt, L., 2018. Clustering and increased settling speed of oblate particles at finite Reynolds number. J. Fluid Mech. 848, 696–721.
Fornari, W., Picano, F., Brandt, L., 2016. Sedimentation of finite-size spheres in quiescent and turbulent environments. J. Fluid Mech. 788, 640–669.
Fornari, W., Zade, S., Brandt, L., Picano, F., 2019. Settling of finite-size particles in turbulence at different volume fractions. Acta Mech 230 (2), 413–430.
Garside, J., Al-Dibouni, M.R., 1977. Velocity-voidage relationships for fluidization and sedimentation in solid-liquid systems. Ind. Eng. Chem. Process Des. Dev. 16 (2), 206–214.
Guazzelli, É., Morris, J.F., 2011. A Physical Introduction to Suspension Dynamics, 45. Cambridge University Press.
Haque, S., Lashgari, I., Giannetti, F., Brandt, L., 2012. Stability of fluids with shear-dependent viscosity in the lid-driven cavity. J. Nonnewton Fluid Mech. 173, 49–61.
Hsu, J.-P., Shie, C.-F., Tseng, S., 2005. Sedimentation of a cylindrical particle in a Carreau fluid. J. Colloid Interface Sci. 286 (1), 392–399.
Izbassarov, D., Rosti, M.E., Niazi Ardekani, M., Sarabian, M., Hormozi, S., Brandt, L., Tammisola, O., 2018. Computational modeling of multiphase viscoelastic and elastoviscoplastic flows. Int. J. Numer. Methods Fluids 88 (12), 521–543.
Janoschek, F., 2013. Mesoscopic Simulation of Blood and General Suspensions in Flow. Eindhoven University of Technology Phd thesis.
Johnson, A.A., Tezduyar, T.E., 1996. Simulation of multiple spheres falling in a liquid-filled tube. Comput. Methods Appl. Mech. Eng. 134 (3), 351–373.
Joseph, D., Liu, Y., Poletto, M., Feng, J., 1994. Aggregation and dispersion of spheres falling in viscoelastic liquids. J. Nonnewton Fluid Mech. 54, 45–86.
Kelessidis, V.C., 2004. An explicit equation for the terminal velocity of solid spheres falling in pseudoplastic liquids. Chem. Eng. Sci. 59 (21), 4437–4447.
Kulkarni, P.M., Morris, J.F., 2008. Suspension properties at finite Reynolds number from simulated shear flow.. Phys. Fluids 20, 040602.
Ladd, A.J., 1993. Dynamical simulations of sedimenting spheres. Phys. Fluids A 5 (2), 299–310.
Lambert, R., Picano, F., Breugem, W.P., Brandt, L., 2013. Active suspensions in thin films: nutrient uptake and swimmer motion. J. Fluid Mech. 733, 528–557.
Lashgari, I., Picano, F., Breugem, W.P., Brandt, L., 2016. Channel flow of rigid sphere suspensions:particle dynamics in the inertial regime. Int. J. Multiph. Flow 78, 12–24.
Malhotra, S., Sharma, M.M., 2012. Settling of spherical particles in unbounded and confined surfactant-based shear thinning viscoelastic fluids: an experimental study. Chem. Eng. Sci. 84, 646–655.
Morrison, F., 2001. Understanding Rheology, first ed. Oxford University Press, Inc., New York.
Nicolai, H., Herzhaft, B., Hinch, E., Oger, L., Guazzelli, E., 1995. Particle velocity fluctuations and hydrodynamic self-diffusion of sedimenting non-Brownian spheres. Phys. Fluids 7 (1), 12–23.
Nouar, C., Bottaro, A., Brancher, J.P., 2007. Delaying transition to turbulence in channel flow: revisiting the stability of shear-thinning fluids. J. Fluid Mech. 592, 177–194.
Peysson, Y., Guazzelli, E., 1998. An experimental investigation of the intrinsic convection in a sedimenting suspension. Phys. Fluids 10 (1), 44–54.
Picano, F., Breugem, W.-P., Brandt, L., 2015. Turbulent channel flow of dense suspensions of neutrally buoyant spheres. J. Fluid Mech. 764, 463–487.
Pignatel, F., Nicolas, M., Guazzelli, E., 2011. A falling cloud of particles at a small but finite Reynolds number. J. Fluid Mech. 671, 34–51.
Putz, A., Burghelea, T., Frigaard, I., Martinez, D., 2008. Settling of an isolated spherical particle in a yield stress shear thinning fluid. Phys. Fluids 20 (3), 33102.
Rajitha, P., Chhabra, R., Sabiri, N., Comiti, J., 2006. Drag on non-spherical particles in power law non-Newtonian media. Int. J. Miner. Process. 78 (2), 110–121.
Reynolds, P., Jones, T., 1989. An experimental study of the settling velocities of single particles in non-Newtonian fluids. Int. J. Miner. Process. 25 (1–2), 47–77.
Richardson, J., Zaki, W., 1954. The sedimentation of a suspension of uniform spheres under conditions of viscous flow. Chem. Eng. Sci. 3 (2), 65–73.
Shah, S.N., El Fadili, Y., Chhabra, R., 2007. New model for single spherical particle settling velocity in power law (visco-inelastic) fluids. Int. J. Multiph. Flow 33 (1), 51–66.
Sierou, A., 2002. Accelerated Stokesian Dynamics: Development and Application to Sheared non-Brownian Suspensions. California Institute of Technology Ph. D. thesis.
Sierou, A., Brady, J.F., 2004. Shear-induced self-diffusion in non-colloidal suspensions. J. Fluid Mech. 506, 285–314.
Turton, R., Clark, N., 1987. An explicit relationship to predict spherical particle terminal velocity. Powder Technol. 53 (2), 127–129.
Uhlmann, M., 2005. An immersed boundary method with direct forcing for simulation of particulate flow. J. Comput. Phys. 209, 448–476.
Uhlmann, M., Doychev, T., 2014. Sedimentation of a dilute suspension of rigid spheres at intermediate galileo numbers: the effect of clustering upon the particle motion. J. Fluid Mech. 752, 310–348.
Yin, X., Koch, D.L., 2007. Hindered settling velocity and microstructure in suspensions of solid spheres with moderate Reynolds numbers. Phys. Fluids 19 (9), 93302.
Yu, Z., Phan-Thien, N., Fan, Y., Tanner, R.I., 2002. Viscoelastic mobility problem of a system of particles. J. Nonnewton Fluid Mech. 104 (2–3), 87–124.
Yu, Z., Wachs, A., Peysson, Y., 2006. Numerical simulation of particle sedimentation in shear-thinning fluids with a fictitious domain method. J. Nonnewton Fluid Mech. 136 (2–3), 126–139.
Zhang, G.-D., Li, M.-Z., Xue, J.-Q., Wang, L., Tian, J.-L., 2016. Wall-retardation effects on particles settling through non-Newtonian fluids in parallel plates. Chem. Pap. 70 (10), 1389–1398.